5 Evolution of star clusters in a cosmological tidal field

Based on:
Steven Rieder, Tomoaki Ishiyama, Paul Langelaan, Junichiro Makino, Stephen McMillan and Simon Portegies Zwart
Evolution of star clusters in a cosmological tidal field
Accepted for publication in MNRAS

We present a method to couple N-body star cluster simulations to a cosmological tidal field, using the Astrophysical Multipurpose Software Environment. We apply this method to star clusters embedded in the CosmoGrid dark matter-only ΛCDM simulation. Our star clusters are born at $z = 10$ (corresponding to an age of the Universe of about 500 Myr) by selecting a dark matter particle and initializing a star cluster with 32,000 stars on its location. We then follow the dynamical evolution of the star cluster within the cosmological environment.

We compare the evolution of star clusters in two Milky-Way size haloes with a different accretion history. The mass loss of the star clusters is continuous irrespective of the tidal history of the host halo, but major merger events tend to increase the rate of mass loss. From the selected two dark matter haloes, the halo that experienced the larger number of mergers tends to drive a smaller mass loss rate from the embedded star clusters, even though the final masses of both haloes are similar. We identify two families of star clusters: native clusters, which become part of the main halo before its final major merger event, and the immigrant clusters, which are accreted upon or after this event; native clusters tend to evaporate more quickly than immigrant clusters. Accounting for the evolution of the dark matter halo causes immigrant star clusters to retain more mass than when the z=0 tidal field is taken as a static potential. The reason for this is the weaker tidal field experienced by immigrant star clusters before merging with the larger dark matter halo.

5.1 Introduction

Globular clusters are dense self gravitating systems of a few 10^4 to $\sim 10^6$ stars (Brodie and Strader 2006). With an age of about 12.6 Gyr (Krauss and Chaboyer

2003) they are among the oldest objects in the universe and tend to populate the haloes of galaxies. Their age is consistent with being born between $z = 12$ to 7, which is consistent with the results of ΛCDM simulations (Kravtsov and Gnedin 2005).

From the time the clusters were born on galaxies grow by about a factor 100 in mass via mergers to their current mass, size and morphology (White and Rees 1978; Peacock 1999). The environment in which the globular clusters evolved since their birth has consequently changed quite dramatically over their lifetimes. These changes may have a profound effect on the evolution of star clusters.

Most modern star-cluster simulations take some sort of background potential of the host galaxy into account. This started already in the early 1990s with Chernoff and Weinberg (1990), and soon afterwards became a lively industry. Many simulations have been performed with a fixed tidal limit (Vesperini and Heggie 1997; Portegies Zwart et al. 1998; Giersz 2001) whereas other include some sort of tidal potential with a more fluent description of the tidal field (Gnedin and Ostriker 1997; Takahashi and Portegies Zwart 2000; Lamers et al. 2010). In most of these simulations the cluster orbit was circular and did not change with time. In a few cases the orbit was allowed to be eccentric, but still did not change with time (Baumgardt and Makino 2003; Giersz and Heggie 2011, 2009). The next refinement was the relaxing of the orbital parameters, allowing the cluster orbit to change (Tanikawa and Fukushige 2005, 2010; Praagman et al. 2010; Renaud et al. 2011; Berentzen and Athanassoula 2012; Renaud and Gieles 2013). The evolution of star clusters in a live galactic potential combined with parametrized cluster evolution was studied by Kruijssen et al. (2011), and Matsui et al. (2012) performed simulations in which they resolve the formation of star clusters in a single galaxy merger event.

However, the mass evolution of the parent galaxy is generally ignored in all these simulations, except for the few cases with a galaxy merger (Saitoh et al. 2009; Renaud et al. 2011; Kruijssen et al. 2012; Renaud and Gieles 2013).

In this paper we study the evolution of star clusters in a cosmological environment. The background potential against which the star clusters are evolved, are taken from the CosmoGrid dark-matter only ΛCDM simulation (Portegies Zwart et al. 2010a). We selected two Milky Way like haloes in which the star clusters are simulated. The coupling between the cosmological simulation and the star cluster is realized via the Astrophysical Multipurpose Software Environment (AMUSE) (Portegies Zwart et al. 2009, 2011, 2013; Pelupessy et al. 2013). In these simulations we initialize a total of 30 star cluster at $z = 10$, and evolve them together with the cosmological simulation up to $z = 0$.

5.2 The experimental setup

We simulate star clusters in a ΛCDM environment. We do this in two steps, first by calculating the ΛCDM environment and then using the tidal field from this environment as an external tidal field for the star cluster simulations. We investigate the results of two distinct regions in the ΛCDM environment.

5.2.1 The CosmoGrid N-body simulation

The cosmological simulation employed in this article originates from the CosmoGrid calculation (Portegies Zwart et al. 2010a; Ishiyama et al. 2013), which is a dark matter-only ΛCDM simulation of 2048^3 particles in a $(21\ h^{-1}\mathrm{Mpc})^3$ co-moving cosmological volume. We performed these simulations using the `GreeM` (Ishiyama et al. 2009b, 2012) and `Sushi` (Groen et al. 2011) codes. GreeM is a massively parallel TreePM code based on the implementation of Yoshikawa and Fukushige (2005). The SUSHI code is an extension of the GreeM code, which can run on a planet wide grid of supercomputers. Within both codes, the equations of motion are integrated in co-moving coordinates using the leap-frog scheme with a shared, adaptive timestep. In this simulation each particle has a mass of $1.28 \times 10^5\ \mathrm{M}_\odot$. In total, we have 556 snapshots, separated by dt $\simeq$ 35Myr (for $t < 7.5$Gyr) and dt $\simeq$ 17.5Myr (for $t \geqslant 7.5$Gyr). The CosmoGrid simulation lasted from $z = 65$ to $z = 0$. We employed the following cosmological parameters: $\Omega_0 = 0.3, \lambda_0 = 0.7, h = 0.7, \sigma_8 = 0.8, n = 1.0$. For more details on the simulation see Portegies Zwart et al. (2010a); Ishiyama et al. (2013).

5.2.2 Halo catalogue

We use the halo finder `Rockstar` (Behroozi et al. 2013a) to identify haloes in each snapshot. Rockstar is based on adaptive hierarchical refinement of friends-of-friends groups in six dimensions and allows for the robust tracking of subhaloes. We use the Consistent Trees merger tree code from Behroozi et al. (2013b) to construct the merger history for all haloes identified by Rockstar. We use AMUSE to find the radial density profiles for our haloes.

From the $z = 0$ haloes, we then select two haloes, based on their relative isolation and a mass comparable to that of the Milky-Way Galaxy. The two haloes are quite similar in many respects, but have a different merger history and the number of subhaloes at $z = 0$ is different.

In Figure 5.1, we present the merger history of the two haloes, both schematically and visually. Halo A completes a major merger at around $t = 6.5$ Gyr, the halo it merges with can be seen in the third figure from the top. At the end of the

Table 5.1: Properties of the selected haloes in the final CosmoGrid snapshot.

Halo	$M_{\rm vir}$ $10^{11}\ h^{-1}{\rm M}_\odot$	$R_{\rm vir}$ h^{-1}kpc	$V_{\rm max}$ km/s	$c_{\rm vmax}$	$N_{\rm sub}$	$D_{\rm n}$ h^{-1}Mpc	b/a	c/a
A	6.33	173.8	140.2	3.53	61	6.30	0.81	0.63
B	4.78	159.4	133.1	3.76	29	0.97	0.73	0.68

$M_{\rm vir}$ and $R_{\rm vir}$ are the virial mass and radius (Bryan and Norman 1998), $V_{\rm max}$ is the maximum of the rotation curve, $c_{\rm vmax}$ is the concentration parameter, $N_{\rm sub}$ is the number of subhaloes with a mass larger than $10^8\ h^{-1}{\rm M}_\odot$, $D_{\rm n}$ is the distance of the nearest more massive halo. a, b and c are the principal axes of the halo.

simulation (see Figure 5.4a), it is in the process of merging with another similar-sized halo. Other than that, there is no significant interaction between $t = 6.5$ Gyr and $t = 13.7$ Gyr. By the end of the simulation, halo A is the largest object within a radius of 6.3 h^{-1}Mpc (see Table 5.1). Halo B exists in a denser part of the volume, and as a result more structure is visible in the outskirts of its environment (see Figure 5.4b). By $z = 0$, it is the largest halo within only 0.97 h^{-1}Mpc. During its history, it underwent many small merger events, and one long-lasting major merger event that completed around $t = 11$ Gyr.

In the mass evolution of both haloes (Figure 5.2), the larger merger events are clearly visible. Since the virial mass includes the mass from subhaloes, the mergers are visible here at the start of interaction, rather than at the end as in Figure 5.1.

The halo density profiles at $z = 0$ (see Figure 5.3) are consistent with the haloes described in Ishiyama et al. (2013), with concentration parameters $c_{\rm vmax}$ of 3.53 and 3.76 for haloes A and B respectively. The lower concentration of halo A may be explained by its ongoing major merger event, which causes the halo to have two cores (see Figure 5.4a).

5.2.3 The clusters

We select a total of 30 dark-matter particles from the $z = 0$ snapshot. For both haloes we select 15 particles at random, equally divided over three bins at galactocentric radius $3 \pm 0.05\ h^{-1}$kpc, $6 \pm 0.05\ h^{-1}$kpc and $12 \pm 0.05\ h^{-1}$kpc. These selected particles are considered the globular clusters for which we will calculate the evolution. Since we do not apply further restrictions in the selection criteria, the clusters may (and likely will) have their peri- and apocentres well outside these bins. In Figure 5.5, we show a projection of these particles in the central region of their host halo at $z = 0$.

We locate the selected dark-matter particles at $z = 10$, which corresponds

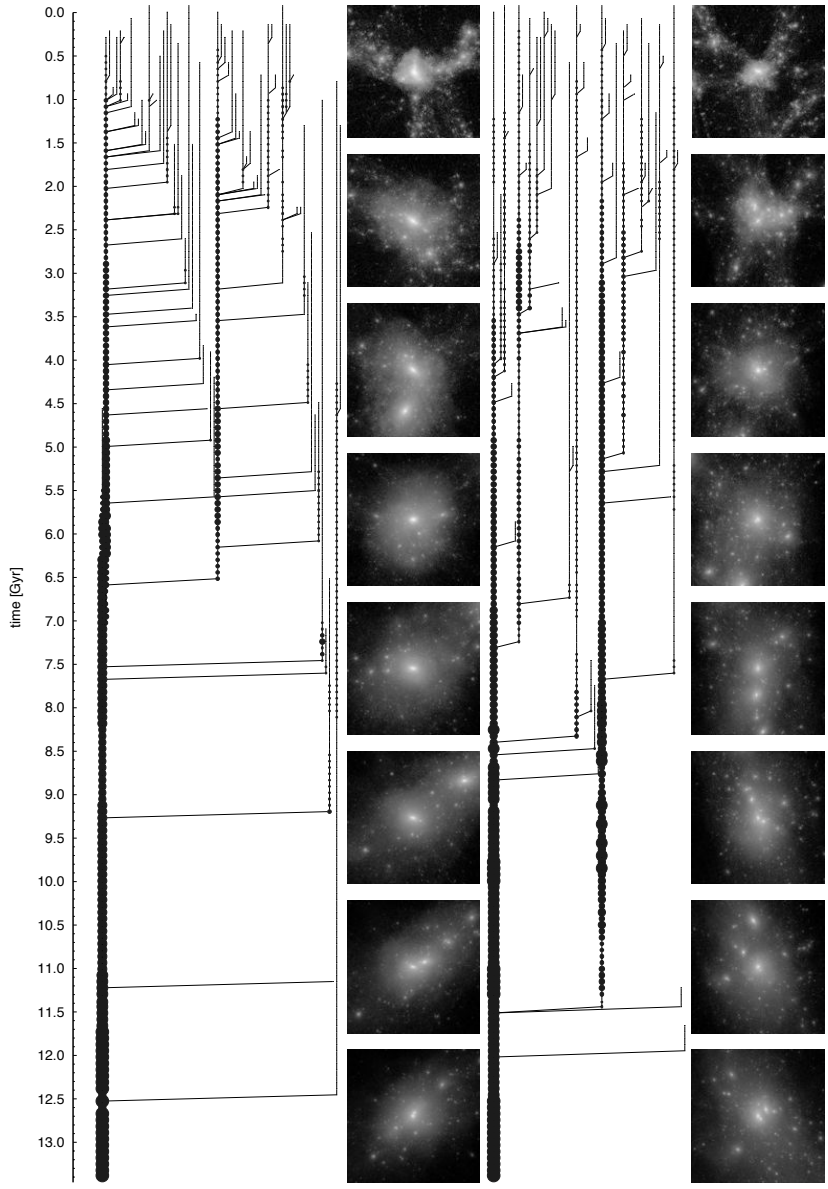

Figure 5.1: The merger history of the two selected dark-matter haloes A (left) and B (right). The size of each circle is proportional to the virial mass of the halo. Only haloes and subhaloes with a peak mass larger than $5 \times 10^8\ h^{-1}\mathrm{M}_\odot$that are accreted at $z = 0$ are plotted. The bottom two halo images are identical to those in Figure 5.4.

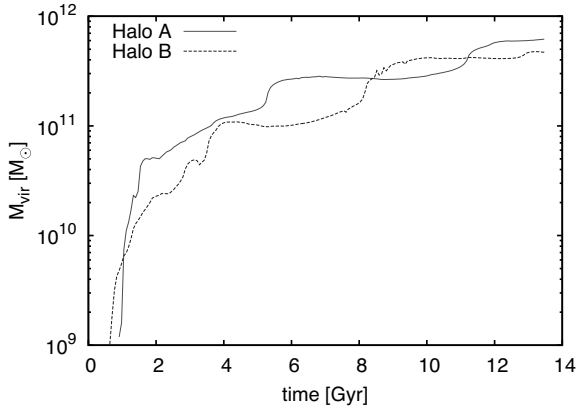

Figure 5.2: Evolution of the virial mass of the two selected haloes A and B. Halo A experiences major merger events around 5 Gyr and 11 Gyr, while halo B experiences a long-lasting major merger event from around 8 Gyr on.

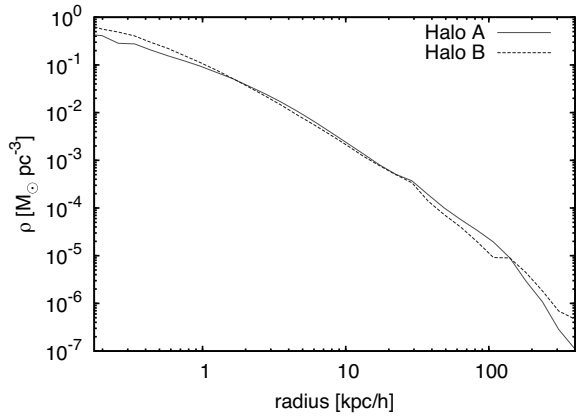

Figure 5.3: Radial density profiles of the two selected haloes A and B and their environment out to $400\ h^{-1}\mathrm{kpc}$ at $z = 0$. The clusters are selected at galactocentric radii of 3, 6 and $12\ h^{-1}\mathrm{kpc}$.

(a) **(b)**

Figure 5.4: Projected image of the two selected haloes A (left panel) and B (right panel), in the final snapshot ($z = 0$). The linear dimension of the image is $400\ h^{-1}\mathrm{kpc}$. The intensity represents the column density (scaled to minimum/maximum values) and the colour is scaled to the velocity dispersion. Each galaxy halo contains about 5 million dark-matter particles.

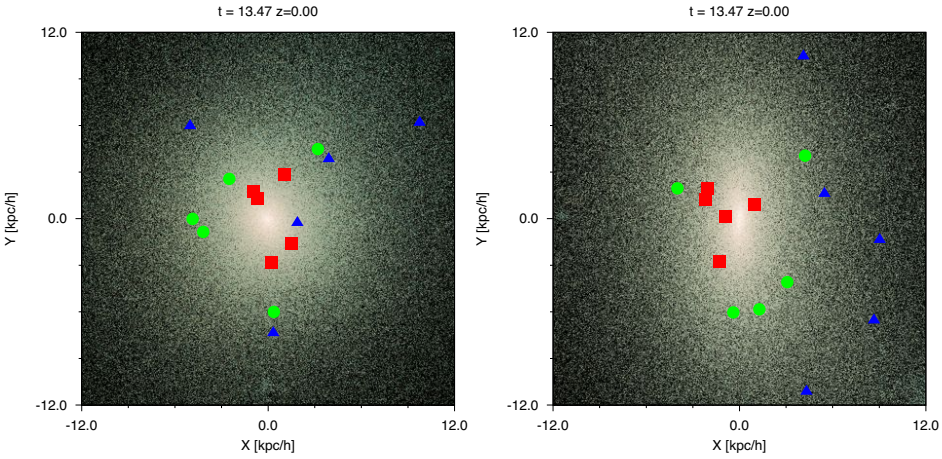

(a) **(b)**

Figure 5.5: Projected image of the central portion of the two selected haloes A (left panel) and B (right panel) with their 'globular clusters' at $z = 0$. The image size is $24\ h^{-1}\mathrm{kpc}$. Red squares indicate clusters at $3\ h^{-1}\mathrm{kpc}$ from the halo centre, green circles those at $6\ h^{-1}\mathrm{kpc}$ and blue triangles those at $12\ h^{-1}\mathrm{kpc}$.

to an age of the universe of ~ 0.5 Gyr. In Figure 5.6 we present the $z = 10$ image of the two selected haloes with their selected dark-matter particles that will represent globular clusters, and the distributions from which these particles are drawn. In both haloes, the particles that end up in the more central parts of the halo are already the most concentrated in density centres at $z = 10$. The particles of halo A are largely concentrated in two regions, in which the haloes that merge around $t = 6.5$ Gyr form. In contrast, the particles of halo B are more spread out, reflecting the more violent history of this halo.

At the $z = 10$ snapshot we initialize a `globular cluster'. Our clusters have 32 000 stars distributed in a Plummer (1911) sphere with a virial radius of 3 pc. The clusters are assumed to be born in virial equilibrium. All stars in the clusters have the same mass and we did not include stellar evolution.

The star clusters are simulated using the AMUSE framework (Portegies Zwart et al. 2009, 2011, 2013; Pelupessy et al. 2013). Our simulation code solves for the equations of motion using `Bonsai` (Bédorf et al. 2012) and `ph4` (McMillan et al. 2012). Bonsai is a Barnes and Hut (1986) tree code that runs on GPUs. It supports both shared timesteps and block timesteps, the latter allowing individual blocks to have different timesteps for increased accuracy in dense regions without slowing the simulation down too much. For this code, we adopted an opening angle (which controls the accuracy, smaller angles being more accurate) of 0.6, we set the smallest timestep to be used to 1/65536 N-body time units (Heggie and Mathieu 1986) and we used a softening length of 0.00125 N-body length units (0.00375 parsec). Ph4 is a direct N-body integrator with block time steps and GPU acceleration. In order to directly compare the results to those obtained with Bonsai, we apply the same softening length as before to the runs with ph4.

In order to validate the use of the tree code, we compare a cluster simulated with Bonsai to a reference simulation using ph4. In Figure 5.7, we present the mass and the Lagrangian radii of this simulated cluster as a function of time, for both Bonsai and ph4.

The difference in mass evolution between ph4 and Bonsai remains quite small until about 5 Gyr. After this moment, both clusters go into core collapse and the two codes start to deviate more. Until about 8.5 Gyr, the ph4 cluster displays much higher mass loss than the Bonsai cluster as it expands following core collapse. After 8.5 Gyr, both codes again show similar behaviour.

The Lagrangian radii of the clusters are nearly equal until core collapse occurs at about 5 Gyr. After this, the core collapse is initially deeper in ph4, while after 8.5 Gyr Bonsai reaches the same depth.

From these results, we infer that our Bonsai simulations are not as well suited for determining the internal structure and evolution of the star clusters as ph4

would be, and underestimates mass loss due to core collapse. However, the effect of the tidal field on the mass loss rate is similar in ph4 and Bonsai. Since we investigate only the mass evolution of the clusters due to the tidal field in this article, we conclude that Bonsai gives an adequate indication of the effect of tidal fields on the cluster mass loss, and that it can be used to study the survivability of star clusters.

5.2.4 The tidal field

In each snapshot of the CosmoGrid simulation we calculate the tidal tensor at the location of the selected dark-matter particle, which represents a star cluster. The contribution to the tidal tensor $\mathbf{T}_\mathrm{t}$ from a particle with relative position $\mathbf{r}$ is given by the second derivative of the gravitational potential ϕ:

$$T_t^{ij}(\mathbf{r}') = -\frac{\partial^2 \phi}{\partial r'^i \partial r'^j} \tag{5.1}$$

where $\mathbf{r}' = \mathbf{r} + \epsilon$. For the CosmoGrid simulation, the value for the softening length ϵ was 175 parsec.

The strength of the tidal field scales as $\frac{\partial^2 \phi}{\partial^2 \mathbf{r}} \sim \frac{1}{r^3}$. Any particle at a distance of about ϵ will have as much effect on the tidal tensor as the largest halo in the CosmoGrid simulation (containing $\sim 3 \times 10^8$ particles) would have at a distance of $\sim$ 117 kpc. We therefore include the contribution from all particles within a radius of 125 kpc from our clusters to determine $\mathbf{T}_\mathrm{t}$.

The strength of the tidal field is calculated from the eigenvalues λ_i and eigenvectors ν_i of this tensor $\mathbf{T}_\mathrm{t}$. The eigenvalues give the magnitude of tidal field, whereas the eigenvectors give the direction along which the system is stretched. This method for calculating the tidal tensor is similar to the one employed in Renaud et al. (2011).

Since we calculate the tidal tensor $\mathbf{T}_\mathrm{t}$ from snapshots of the CosmoGrid simulation and the number of snapshots is limited, we do not have a continuous tidal field. In order to prevent large, sudden changes, we linearly interpolate the tidal tensor between snapshots to create a continuous tidal tensor. In Section 5.2.7, we validate this interpolation method.

5.2.5 Combining the clusters and the tidal field

We use the tidal tensor to calculate the external potential acting on each of the stars in the simulated clusters. We integrate the internal potential of the clusters with this external potential using a Bridge-like scheme (Fujii et al. 2007), which is implemented in AMUSE (Portegies Zwart et al. 2013).

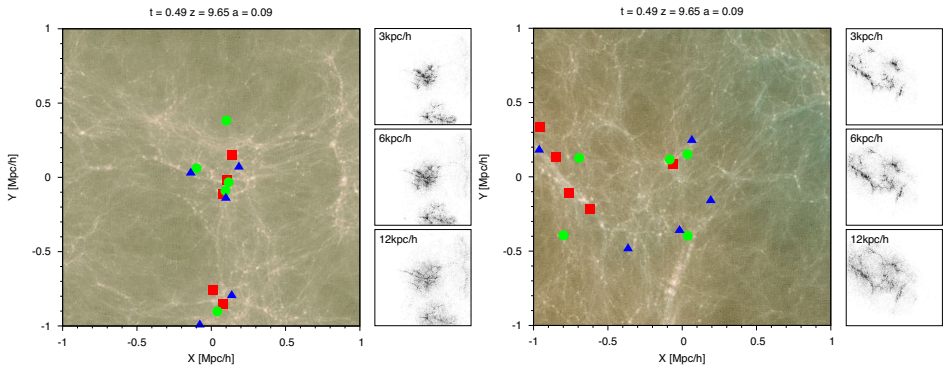

Figure 5.6: Projected image of halo A (left) and B (right) at $z = 9.65$. The image size is $2\ h^{-1}\mathrm{Mpc}$. Red squares indicate clusters that at $z = 0$ were selected at $3\ h^{-1}\mathrm{kpc}$ from the halo centre, green circles those at $6\ h^{-1}\mathrm{kpc}$ and blue triangles those at $12\ h^{-1}\mathrm{kpc}$. The panels on the right display (from top to bottom) the distributions of particles that end up in spherical shells at 3, 6 and $12\ h^{-1}\mathrm{kpc}$ from the halo centres at $z = 0$.

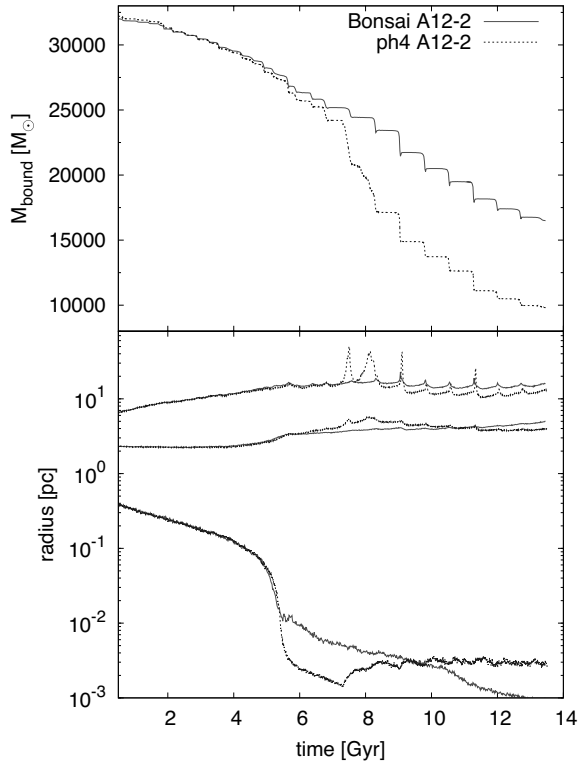

Figure 5.7: Evolution of the bound mass (top panel) and the 90%, 50% and 1% Lagrangian radii (top to bottom, bottom panel) of star cluster A12-2. The cluster was simulated with Bonsai (solid curves) and ph4 (dashed curves).

This scheme can be used to combine interacting systems that are calculated in different instances and/or using different codes, i.e. multiple interacting star clusters, globular clusters in a galactic environment, a galactic disk in a halo potential or embedded star clusters (Pelupessy and Portegies Zwart 2011).

In this scheme, the cluster experiences the gravity from the external field through periodic velocity kicks. It alternates between these velocity kicks and a drift due to self gravity evolution of the system. During one time step, the system first experiences a kick of the velocities over a time step $dt/2$, then a drift over a time step dt, and finally another kick over $dt/2$. In our setup, the external potential is derived from the CosmoGrid simulation and therefore necessarily fixed, while the clusters receive velocity kicks from the external tidal field.

5.2.6 Escaping and bound stars

In the simulations, we calculate a tidal radius from the cluster mass and the strength of the tidal field (given by the largest eigenvalue of the tidal tensor $\lambda_{\rm max}$). This tidal radius is equal to

$$R_{\rm tidal} = \left(\frac{GM}{\lambda_{\rm max}}\right)^{1/3}. \tag{5.2}$$

Particles at a distance from the cluster centre larger than $R_{\rm tidal}$ will experience a larger force from the external tidal field than from the cluster's own internal mass. It is then considered an `escaping particle', and not included in the cluster's bound mass (defined as the total mass inside $R_{\rm tidal}$). If the particle returns to a position within the tidal radius, this is reversed. If it moves to a distance $> 10R_{\rm tidal}$, the particle is removed from the simulation.

At times when the cluster is located in the centre of a local subconcentration of dark matter or near a halocentre, the value of $\lambda_{\rm max}$ may become negative for a short period. In such cases, the tidal radius is not defined. At such times, the bound mass of the cluster is not evaluated and no mass loss is experienced by the cluster. Stars that may have escaped from the cluster during this period will however still be removed once the tidal radius is again defined.

5.2.7 Validation

We validate the simulation environment by comparing our results with those obtained using a different method and to a star cluster in isolation. As a reference model, we simulate a star cluster in an orbit with $R_{\rm apo} = 12\ h^{-1}$kpc and $e = 0.71$ around a point-mass of $10^{10}\ {\rm M}_\odot$, by including this point-mass in the simulation. The simulated cluster contains 8 000 equal-mass stars of $1\ {\rm M}_\odot$within a Plummer (1911) sphere with a virial radius of 3 pc. We compare this model to a simulation

where we first calculated the tidal field that would be experienced by such a cluster and used this as an external field for the simulation using the Bridge scheme. For this test, we run simulations with ph4, as the large difference in particle masses would make the reference simulation unsuitable for a single-precision tree code like Bonsai.

The mass evolution of these test simulations are presented in Figure 5.8. The difference in the mass evolution of the cluster in the simulations with and without Bridge is quite small, indicating the validity of this method for this set of parameters.

Also, we validate the effect of the discretisation at which the tidal tensor is evaluated. Since the time-resolution of the cosmological simulation is limited to about 35 Myr at high z and 17.5 Myr at low z, anomalies will be visible for clusters with an orbital period of this order. Ideally, one would like to increase the number of snapshots for the cosmological simulation in order to obtain a higher time-resolution for the tidal tensor.

In Figure 5.9 we present the mass evolution of a cluster in a static halo potential (Paczynski 1990) with a core mass of 10^9 $\mathrm{M}_\odot$ and a core radius of 1 kpc, now using tidal tensors sampled with a time resolution ranging from 1 to 35 Myr. The orbital parameters of the cluster in this potential are $R_{\mathrm{apo}} = 15\,\mathrm{kpc}$, $e = 0.85$, and the cluster orbits the potential in 670 Myr. The mass loss rates for the clusters using a tidal tensor sampled with a time interval of 1 Myr and 9 Myr have converged in this orbit, while the clusters using tensors sampled with a 17.5 or 35 Myr time interval show a slightly reduced mass loss rate and therefore longer lifetimes. For clusters with closer orbits, this effect will be stronger. In a cosmological setting, any change in the potential that takes place on a timescale similar to or smaller than the sampling rate cannot be taken into account properly, and may also lead to errors in the mass loss rate.

5.3 Results

5.3.1 The evolution of the selected haloes

We perform simulations of star clusters in two selected haloes, which we call halo A and halo B. Halo A experiences two major merger events, the last of which is not completed by $z = 0$ (see Figures 5.1 and 5.2), but otherwise its evolution is rather gradual from $z = 65$ to $z = 0$. By the end of the simulation (at $z = 0$) its mass is $6.3 \times 10^{11}\ h^{-1}\mathrm{M}_\odot$.

Halo B has a more violent history; it experiences two major mergers, one between 4 Gyr and 5 Gyr and one with comparable mass between 8 Gyr and 10 Gyr

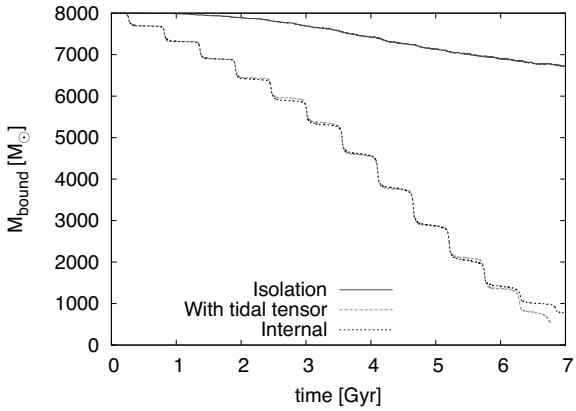

Figure 5.8: Mass evolution of a 8 000 star cluster in isolation (solid curve), and in orbit around a point mass of 10^{10} $\mathrm{M}_{\odot}$(dashed and dotted curves). The dashed curve gives the mass-evolution of the cluster when the tidal field is incorporated in the gravitational N-body simulation using Bridge. The tidal field in the latter case was resolved at the resolution of the N-body integrator. The dotted curve gives the mass-evolution when the point mass is directly included in the simulation.

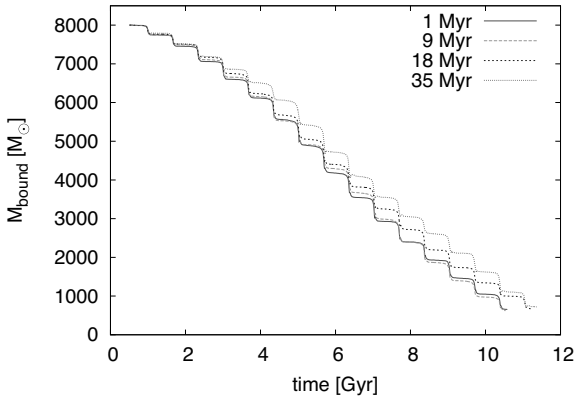

Figure 5.9: Mass evolution of a 8 000 star cluster with tidal field calculated from a halo potential using the tidal tensor and evaluated using Bridge at discrete time intervals. The cluster orbits in the halo potential with $R_{\mathrm{apo}} = 15\,\mathrm{kpc}$ and $e = 0.85$. In order to study the effect of the time resolution of the tidal field, we evaluate the tidal tensor with time intervals of 1, 9, 18 and 35 Myr.

(see also Figures 5.1 and 5.2). By the end of the simulation at $z = 0$ it has a mass of $4.8 \times 10^{11}\ h^{-1}\mathrm{M}_{\odot}$ (see Table 5.1). Even though the total mass of halo B is slightly smaller than that of halo A, both haloes contain a mass of $7 \times 10^{9}\ h^{-1}\mathrm{M}_{\odot}$ within 3 kpc from the halo centre (see Figure 5.3).

In each halo we have selected 15 dark-matter particles which are initialized at $z = 10$ as star clusters, and evolved with the cosmological simulation as a background potential.

5.3.2 The evolution of the star clusters

We perform 30 simulations of star clusters with a tidal field; 15 are initialized in halo A and 15 in halo B. An additional cluster is simulated in isolation, to identify the mass loss component caused by relaxation. For this cluster, a radius of 200 pc is used to determine if stars are bound. All clusters are born at $z = 10$ (corresponding to an age of the Universe of about 500 Myr) with a total mass of $\sim 32\,000\ \mathrm{M}_{\odot}$ and an initial virial radius of 3 parsec for each cluster. All stars have the same mass and we did not include stellar evolution.

In Figure 5.12 and Table 5.2 we present the mass evolution and final masses of these simulations. The mass evolution of all simulated clusters is rather gradual irrespective of the sudden events in the growth of the host haloes. The small and rather sudden changes in mass are caused by the pericentre passages of the clusters in its orbit around the dark matter host. The clusters with a smaller orbital separation at z=0 tend to lose mass at a higher rate.

The averaged final mass of the star clusters in halo A is smaller than the final mass of those that evolved in halo B for each of the radial bins (see Table 5.2). This is consistent with halo B originating from a larger number of less massive haloes, causing the tidal forces experienced by clusters in this halo over time to be smaller. For both haloes the clusters selected around $3\ h^{-1}$kpc show the strongest mass loss; this is noticeable from the first few Gyr on. This behaviour is as expected from the distribution of particles at $z = 10$ (see Figure 5.6), where we see that the particles that end up in the central parts are already more concentrated at high redshift. The rate of mass loss for these clusters proceeds more gradual compared to the clusters in wider orbits. Integrated over time clusters lose mass at a rather constant rate.

In Table 5.2 we distinguish between two types of clusters: those that were part of the main halo before the final completed major merger event (at $t = 6$ Gyr and $t = 8$ Gyr for haloes A and B, respectively), and those that are accreted upon or after this event. The former we identify with `native' clusters, and the others as `immigrants'. The difference between immigrant clusters and native clusters is apparent in Figure 5.10.

In Figure 5.10 we present the orbital evolution of the selected dark-matter

Table 5.2: Results for star cluster simulations using Bonsai, with various tidal tensors. Each cluster contains 32 000 equal mass stars of about 1 $M_\odot$, and has an initial radius of 3 parsec. We use a softening length of $40/N$. Cluster type is Immigrant (I) or Native (N). The clusters indicated with a bold font are displayed in Figures 5.11 and 5.14.

Cluster ID	Halo	Type	Distance at z=0	Mass at z=0
Isolated				**28174 $M_\odot$**
A3-1	A	I	3 h^{-1}kpc	10157 $M_\odot$
A3-2	A	I	3 h^{-1}kpc	15171 $M_\odot$
A3-3	A	N	3 h^{-1}kpc	10969 $M_\odot$
A3-4	A	N	3 h^{-1}kpc	11085 $M_\odot$
A3-5	A	N	3 h^{-1}kpc	10169 $M_\odot$
Average				**11510 $M_\odot$**
A6-1	A	I	6 h^{-1}kpc	17906 $M_\odot$
A6-2	A	N	6 h^{-1}kpc	24130 $M_\odot$
A6-3	A	N	6 h^{-1}kpc	14964 $M_\odot$
A6-4	A	N	6 h^{-1}kpc	17978 $M_\odot$
A6-5	A	N	6 h^{-1}kpc	18430 $M_\odot$
Average				**18682 $M_\odot$**
A12-1	A	I	12 h^{-1}kpc	21677 $M_\odot$
A12-2	A	I	12 h^{-1}kpc	16487 $M_\odot$
A12-3	A	N	12 h^{-1}kpc	17574 $M_\odot$
A12-4	A	N	12 h^{-1}kpc	15873 $M_\odot$
A12-5	A	N	12 h^{-1}kpc	16904 $M_\odot$
Average				**17703 $M_\odot$**
B3-1	B	I	3 h^{-1}kpc	19422 $M_\odot$
B3-2	B	N	3 h^{-1}kpc	18974 $M_\odot$
B3-3	B	N	3 h^{-1}kpc	16366 $M_\odot$
B3-4	B	N	3 h^{-1}kpc	15633 $M_\odot$
B3-5	B	N	3 h^{-1}kpc	20839 $M_\odot$
Average				**18247 $M_\odot$**
B6-1	B	I	6 h^{-1}kpc	24774 $M_\odot$
B6-2	B	N	6 h^{-1}kpc	18446 $M_\odot$
B6-3	B	I	6 h^{-1}kpc	15988 $M_\odot$
B6-4	B	N	6 h^{-1}kpc	21128 $M_\odot$
B6-5	B	N	6 h^{-1}kpc	21398 $M_\odot$
Average				**20347 $M_\odot$**
B12-1	B	I	12 h^{-1}kpc	19986 $M_\odot$
B12-2	B	I	12 h^{-1}kpc	23479 $M_\odot$
B12-3	B	N	12 h^{-1}kpc	25819 $M_\odot$
B12-4	B	N	12 h^{-1}kpc	26374 $M_\odot$
B12-5	B	I	12 h^{-1}kpc	22137 $M_\odot$
Average				**23559 $M_\odot$**

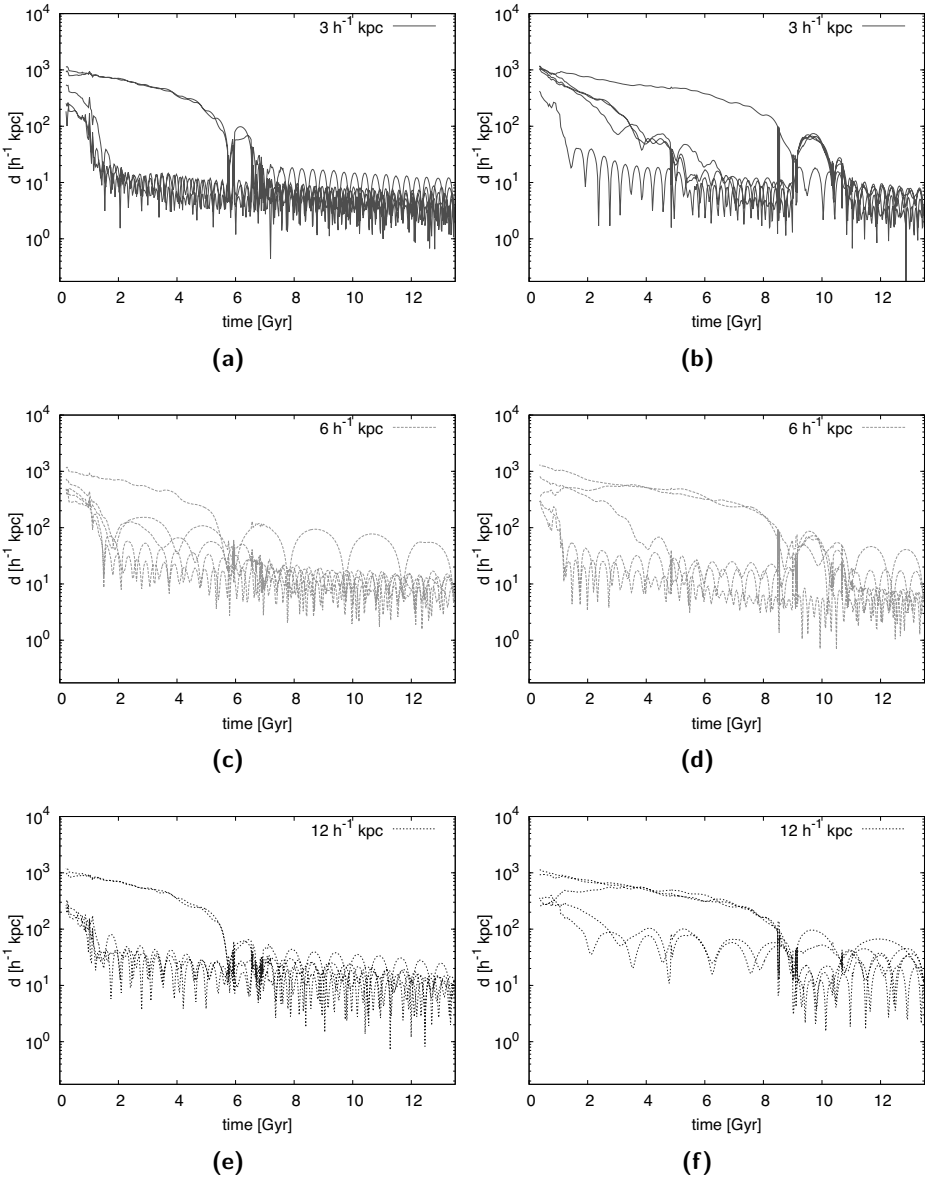

Figure 5.10: Co-moving distance of the clusters to the main halo centre for clusters in halo A (left) and halo B (right). Top, middle and bottom figures show clusters selected at 3, 6 and $12\ h^{-1}\mathrm{kpc}$, respectively. Merger events in both haloes are visible as particles fall towards the halo centre. The orbital periods of the clusters are clearly visible.

particles (i.e. the clusters) from halo A (left) and halo B (right). In the following paragraphs, we discuss the evolution of two clusters from each halo; one immigrant and one native cluster in more detail.

The clusters in halo A

In Figure 5.11, we show the mass evolution, mass loss rate over intervals of 10 Myrs and tidal field strength for an immigrant cluster (nr. A6-1, left) and a native cluster (nr. A6-4, right). This halo experiences a major merger which starts at about 6 Gyr, at that time the immigrant cluster is also captured by the main halo. The merger lasts until about 8 Gyr (see also Figure 5.1). When the merger is finished, the tidal field strength $\lambda_{\max}$ shows more frequent peaks, indicating it has a shorter orbital period than before the merger. However, there is little change in the mass-loss rate.

The native cluster of halo A experiences the same merger but was already member of the major halo. Its orbit becomes somewhat less eccentric after the merger, while its apocentric distance and orbital period decrease. The mass-loss rate from this cluster is mostly unaffected by the merger.

In Figure 5.13, we show the result of two star clusters (A12-1 and A12-4), both using the tidal tensor calculated from the evolving CosmoGrid halo and using a tidal tensor calculated from the static $z = 0$ CosmoGrid halo. For the static halo case, we sampled the tensor using the orbital trajectory of the cluster around its parent halo. For the native cluster, the resulting mass evolution differs only marginally, while the immigrant cluster suffers considerably higher mass loss in the static halo case, especially around the time the halo merger takes place, when its orbit is erratic. The static halo is a good approximation for the native cluster, while it falls short for the immigrant cluster.

The clusters in halo B

In Figure 5.14 we present the details of the evolution of an immigrant cluster (nr. B6-3, left) and a native cluster (nr. B6-2, right) of halo B. The immigrant cluster is captured during the major merger event that starts around $t = 8\,\mathrm{Gyr}$. Different from the clusters in halo A, the orbital period of the cluster around the dark matter halo is hardly visible in the cluster's mass evolution (see Figure 5.14, left, top panel). Just before the merger (around $t = 7\,\mathrm{Gyr}$) the mass-loss rate is slightly smaller than before or after the merger. This is caused by the distortion of the infalling halo of which this cluster is a member at that time. When the merger is completed the cluster mass-loss rate has resumed to be as high as before the merger (see Figure 5.14, left, second panel).

The native cluster becomes part of the main halo during its first major merger,

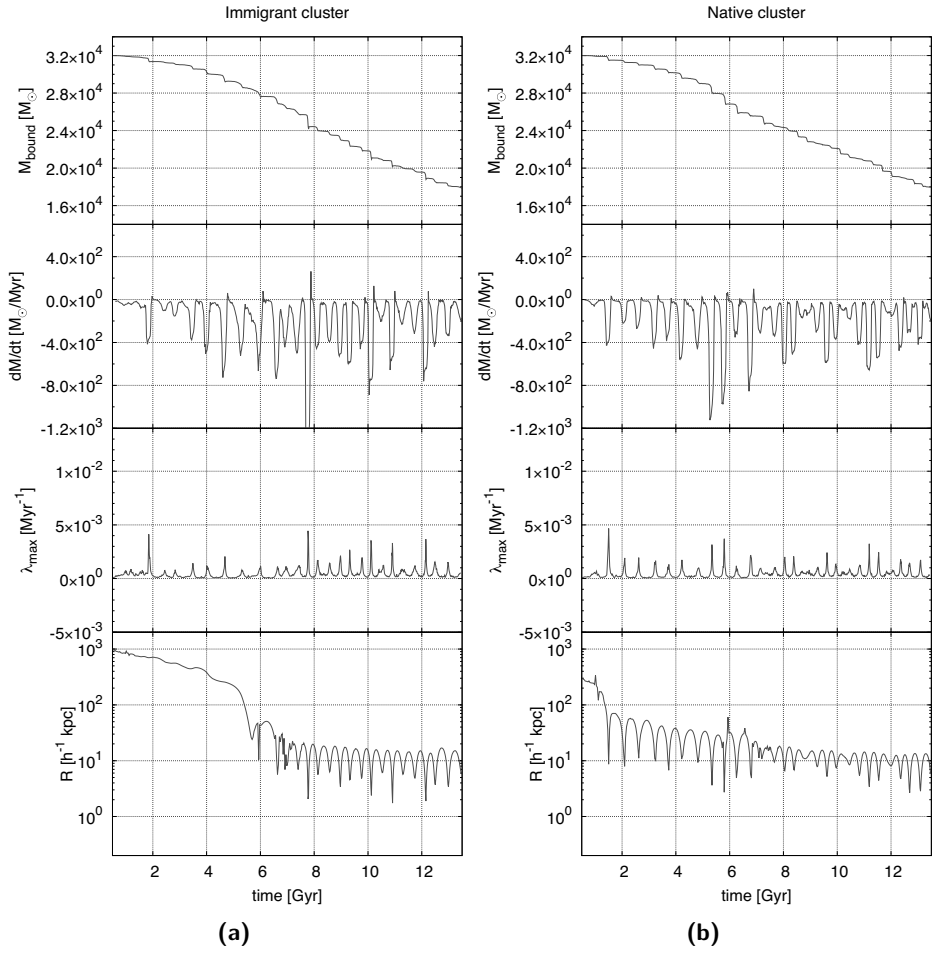

Figure 5.11: Evolution of two star clusters in orbit around halo A. To the left is a typical immigrant cluster identified with dark-matter particle nr A6-1 and to the right we present a native cluster, particle nr A6-4 (see also Table 5.2). From top to bottom the panels show the bound mass, the mass-loss rate, the strength of the tidal field ($\lambda_{\max}$) and the co-moving distance of the cluster to the centre of the dark matter halo.

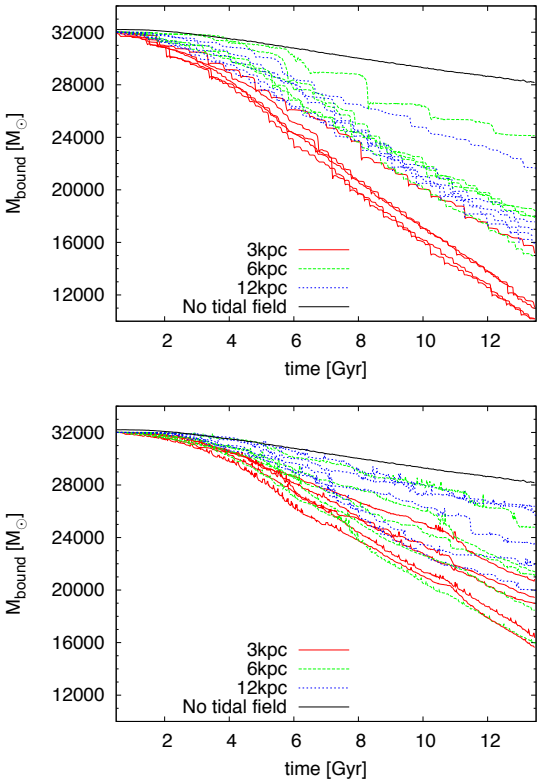

Figure 5.12: Bound mass in the simulated clusters for haloes A (top figure) and B (bottom figure). The red, solid; green, dashed and blue, dotted lines indicate clusters selected at 3, 6 and 12 $h^{-1}\mathrm{kpc}$, respectively. The black line indicates the mass of a cluster without an external tidal field.

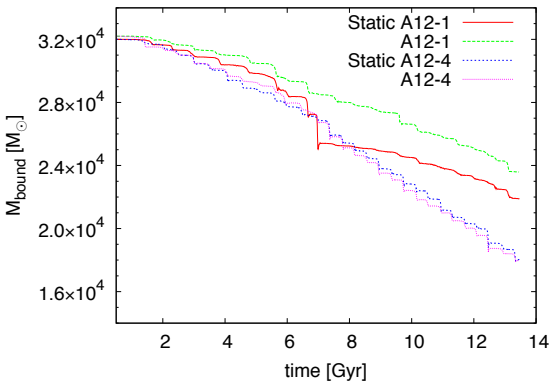

Figure 5.13: Evolution of two star clusters A12-1 (immigrant) and A12-4 (native). Both are simulated in an evolving halo as well as a static halo.

at around $t = 5$ Gyr. After this merger, the tidal forces experienced by the cluster are stronger than before, visible in Figure 5.14 (right, third panel) as a sudden increase of λ_{max} after $t = 6$ Gyr. Its mass-loss rate is also increased, as can be seen from Figure 5.14 (right, second panel) and the difference in slope of $M_{\text{bound}}(t)$ at $t = 4$ Gyr and $t = 8$ Gyr. The second major merger event leads to a temporary reduction in mass-loss for the cluster (at around $t = 10$ Gyr). After this second halo merger the orbital period is evidently visible in the mass evolution of the cluster.

5.4 Discussion and conclusions

We presented a method to simulate star clusters within a pre-calculated tidal field, using the AMUSE environment. As a proof of concept, we apply this method to calculate the mass loss rates for star clusters in two live ΛCDM haloes from the CosmoGrid simulation. Our method compares well to self-consistent simulations.

We find that the mass loss rate strongly depends on the cluster's orbital parameters around the halo centre, as well as the central mass of the halo. Also, tidal disruption due to the ΛCDM environment is weaker in haloes that experienced many mergers. Finally, we find that in a Milky Way-like halo, the contribution of the ΛCDM environment to $\Delta M/M_{\text{init}}$ can be up to 0.6 for clusters with an initial mass of 32 000 $M_\odot$.

In this article, several effects have not been taken into account, most notably we used a dark matter-only simulation. In this section, we discuss the relevance of these effects and how we intend to address these shortcomings.

Since the CosmoGrid simulation is a dark matter-only simulation, we do not account for the effect of baryons. Because the formation of the large-scale environment is dominated by dark matter, the lack of baryons has little influence on the formation of the haloes. Star clusters however likely contain little or no dark matter (Baumgardt et al. 2010; Conroy et al. 2011).

Because our simulation lacks baryons, there is no indication where star clusters would have formed or ended up had they been formed in our cosmological environment. We therefore have to resort to our method of identifying tracer particles for the star clusters in the final snapshot. We selected particles based on their distance to the halo centre. However, it is very likely that globular clusters would have formed in more specific locations, and possibly followed paths quite different from the ones in our simulation. In a simulation that includes baryonic matter and star formation, it would be possible to detect locations and masses of star clusters as they form.

The difference between old and young clusters herein is large: old clusters (like

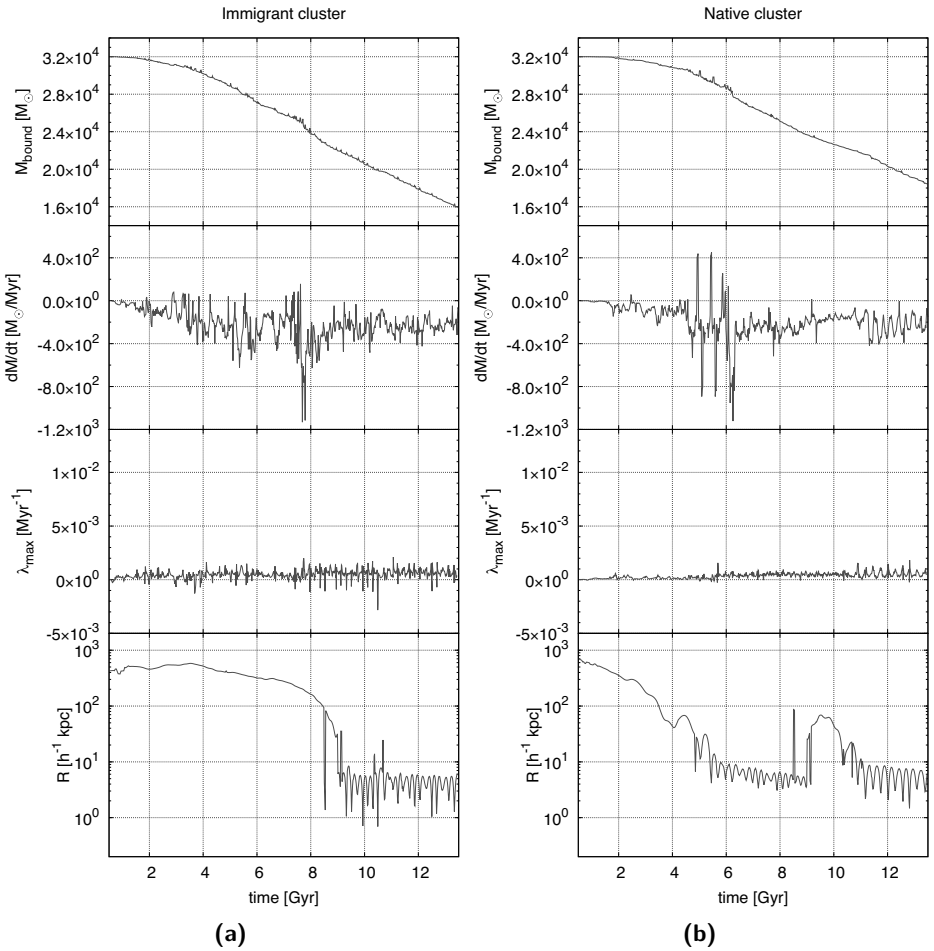

Figure 5.14: Evolution of two star clusters in orbit around halo B. To the left is a typical immigrant cluster identified with dark-matter particle nr B6-3 and to the right we present a native cluster, particle nr B6-2 (see also Table 5.2). From top to bottom the panels show the bound mass, the mass-loss rate, the strength of the tidal field ($\lambda_{\rm max}$) and the co-moving distance of the cluster to the centre of the dark matter halo. Negative values of $\lambda_{\rm max}$ correspond to times where the cluster is located inside a local (sub)concentration of matter. The spikes in the bottom panels for the immigrant and the native clusters is associated with a confusion in identifying the main parent in the halo finder.

the globular clusters in the Milky Way) formed before there was a Galactic disk, and remain relatively free of its influence. Young clusters however form in the galactic disk, and the tides experienced by these clusters are dominated by encounters with giant molecular clouds and spiral arms (Lamers and Gieles 2006; Gieles et al. 2007), the effect of which is about four times larger than the tidal field (e.g. Lamers and Gieles 2006, Figure 1). For this reason, we focus on old stellar clusters and initialize our simulated star clusters at an early epoch, before the galactic environment would have formed. In order to simulate young clusters, a galaxy simulation including baryons would be required. However, when the old clusters formed, the GMC density in the star-forming environment was likely very high, causing early disruption of low-mass globular clusters (Elmegreen 2010). This effect is not included in our simulations.

In order to investigate a large number of clusters with a reasonable amount of stars, we used the Barnes and Hut (1986) tree code `Bonsai` for most of our star cluster simulations. We compared the results for two distinct star clusters to similar simulations with the direct N-body code `ph4`. The results for both runs are similar for both codes, the direct code showing enhanced mass loss around the time of core collapse. However, the tree code fails to accurately describe the inner structure of the star cluster, and requires the distance between stars to be softened.

Another limit of our environment is its resolution. The spatial resolution of CosmoGrid is given by the softening length employed (175 parsec). Forces that occur on a scale similar to or smaller than this softening length are not accurately taken into account. Likewise, the mass resolution of dark matter particles in CosmoGrid is 1.28×10^5 $M_\odot$, about 4 times larger than the initial mass of our simulated clusters. The effects of tidal forces caused by a small dark matter object passing at close range to our clusters (such as a subhalo) are therefore limited, creating a possible bias against the effect of such structures. However, this resolution effect would be more important for baryons than it is for dark matter.

The benefit of using a large-scale cosmological simulation however, is that the formation of a dark-matter halo is followed. A simulation that only models a collision between galaxies would not take the earlier history and distribution of star clusters into account. In order to have the benefits of both a cosmological environment and high resolution, one could use re-simulation, where galaxies are simulated at high resolution within a lower-resolution environment.

Another limit imposed by our use of a pre-calculated simulation is its limited number of snapshots. We lack continuous information about the tidal tensor. In order to prevent sudden changes in the tidal field, we interpolate the tidal tensor between snapshots. However, it remains impossible to accurately track sudden changes in the tidal field on timescales shorter than our time resolution, such

as those occurring during halo mergers. Since the orbital periods of our clusters around the halo centre are larger than this time resolution, we do not expect this to have a large influence on the evolution of the tidal field. However, short-lasting passages of nearby objects may not be taken into account accurately, and a method in which the tidal field is sampled at more intervals remains preferable.

In a follow-up article (Rieder et al., in prep.), we will apply the method described in this article to the evolution of star clusters in the disk of a simulated Milky Way-type galaxy. In this follow-up, we will address several of the limitations discussed above, especially the lack of baryons and as a result the orbits and origins of the clusters.

Acknowledgements

It is our pleasure to thank the anonymous referee for very helpful suggestions and comments that greatly helped to improve the article. Also, we are grateful to Arjen van Elteren, Derek Groen, Inti Pelupessy, Jeroen Bédorf, Mark Gieles and Nathan de Vries for support, interesting discussions and useful suggestions.

This work was supported by NWO (grants IsFast [#643.000.803], VICI [#639.073.803], LGM [#612.071.503] and AMUSE [#614.061.608]), NCF (grants [#SH-095-08] and [#SH-187-10]), NOVA and the LKBF in the Netherlands, and by NSF grant AST-0708299 in the U.S. T.I. is financially supported by MEXT HPCI STRATEGIC PROGRAM and MEXT/JSPS KAKENHI Grant Number 24740115. We thank the DEISA Consortium (EU FP6 project RI-031513 and FP7 project RI-222919) for support within the DEISA Extreme Computing Initiative (GBBP project).

The Cosmogrid simulations were partially carried out on Cray XT4 at Center for Computational Astrophysics, CfCA, of National Astronomical Observatory of Japan; Huygens at the Dutch National High Performance Computing and e-Science Support Center, SurfSARA (The Netherlands); HECToR at the Edinburgh Parallel Computing Center (United Kingdom) and Louhi at IT Center for Science in Espoo (Finland).